IEEE Access
Multidisciplinary ⋮ Rapid Review ⋮ Open Access Journal

Received June 16, 2021, accepted August 24, 2021, date of publication August 30, 2021, date of current version September 9, 2021.

Digital Object Identifier 10.1109/ACCESS.2021.3108663

The Improved Equivalent Circuit Models Considering End Effects of Annular Linear Induction Electromagnetic Pump for Space Nuclear Power Supply

ZHENYANG ZHANG[1], (Member, IEEE), HUIJUAN LIU[1], (Member, IEEE), TENGFEI SONG[1], QIAN ZHANG[1], (Student Member, IEEE), LIXIN YANG[2], AND KEMING BI[3]

[1]School of Electrical Engineering, Beijing Jiaotong University, Beijing 100044, China
[2]School of Mechanical, Electronic and Control Engineering, Beijing Jiaotong University, Beijing 100044, China
[3]Division of Reactor Engineering Technology Research, China Institute of Atomic Energy, Beijing 102413, China

Corresponding author: Huijuan Liu (hjliu@bjtu.edu.cn)

This work was supported in part by the National Natural Science Foundation of China under Grant 51377008, and in part by the Horizontal Project of Beijing Jiaotong University under Grant M20GY00030.

ABSTRACT The improved equivalent circuit models considering the end effects are put forward to predict the performance of annular linear induction electromagnetic pump (ALIP) based on the one-dimensional analytical model built in this paper. First, the one-dimensional physical model of ALIP is established, and the analytical expressions of electromagnetic fields are deduced and the impact of the end effects on it is analyzed. Then, two equivalent circuit models including the model only considering the end effects and the model fully taking the end effects and the difference of synchronous velocity among the end effect traveling waves and the fundamental wave into account are developed. Meanwhile, the key impedance parameters in the equivalent circuit models are obtained and the correction coefficients of the impedance generated by the end effects are abstracted. Furtherly, the performances of a small designed ALIP are calculated by the conventional and two improved equivalent circuit models respectively, the results obtained from them are compared with measured data to validate the rationality and feasibility of the models proposed.

INDEX TERMS ALIP, electromagnetic field, equivalent circuit, end effect, developed pressure.

I. INTRODUCTION

Electromagnetic pump (EMP) [1] plays an important role in the cooling process of the liquid metal cooled nuclear reactor and space nuclear reactor power supply [2]–[4]. Compared with conventional mechanical pumps, EMP transmits liquid metal through Lorentz force, so there is no need for rotating shafts, gears, impellers and other mechanical transmission components. This means that it has natural advantages in terms of sealing, safety and economy [5]. ALIP, as a special form of EMP, has better structural symmetry, and is more suitable for ordinary piping systems, then the annular channel can also improve output stability to a certain extent. Moreover, the current in the liquid metal of ALIP is induced by an alternating magnetic field originated from the excitation windings, thereby the inherent problems associated with electrode corrosion of the conduction EMPs are virtually nonexistent [6]. Based on these advantages, ALIP has emerged as the preferred choice for the liquid metal cooled reactors.

The ALIP can be totally regarded as a short-primary tubular linear induction motor (TLIM) when the liquid metal fluid being transported is considered as superior conductive solid moving at a time-average velocity. As a result, it is feasible and reasonable to analyze the electromagnetic properties of ALIP with the theory of linear induction motors (LIMs) [7]–[9]. At present, with the theory of LIMs, a lot of research works have been carried out for the characteristic prediction of ALIP in the design stage.

Based on the basic equivalent circuit model of the tube linear induction motor (TLIM) established by Nasar in [8], Baker and Tessier derived the equivalent circuit parameters and electromagnetic pressure expression of ALIP, then

The associate editor coordinating the review of this manuscript and approving it for publication was Lei Zhao.

proposed an end effects coefficient related to the number of poles to correct the expression [1].

Following up on the direction of the equivalent circuit, Kim and Kwak have obtained the analytical expression of developed pressure via introducing the major hydraulic pressure loss calculated by Darcy–Weisbach equation and minor hydraulic pressure loss calculated by the empirical coefficient, and discussed the influence of different characteristic parameters on P-Q characteristic curve and efficiency of the electromagnetic pump [10]–[13]. In [14], [15], based on the combination of circuit and magnetic circuit, a new equivalent circuit model for predicting electromagnetic pressure is proposed, whereas the simple end effects coefficient in [1] was still adopted. On this basis, Wang introduced the hydraulic loss including friction pressure loss and form pressure loss, then corrected the electromagnetic pressure by the end correction coefficient of experimental data fitting and carried out the performance optimization design [16]. Although the end effects and saturation problem have been considered in the correction coefficient, this method has some limitations and cannot be applied in the theoretical design stage.

Different from the equivalent circuit method, in [17], [18], the electromagnetic fields characteristics of ALIP were presented based on the Maxwell electromagnetic field equations. In [19], Seong categorized the induced eddy current in the liquid metal as the time derivative term generated by the time-varying magnetic field and the convective term originating from the sodium flow. The magnetic field, the time-varying part of the induced eddy current and the electromagnetic force produced by it were less affected by flow rate, and the convective part and the electromagnetic force produced by it was more affected. In addition, the research indicated that the convective eddy current was the main cause of the end effects and the double supply frequency (DSF) pressure pulsation, and the amplitude of the DSF pressure pulsation was proportional to the flow rate and the end effect in the outlet region was more obvious than the inlet. Kim draw several conclusions that the end effects caused by the finite length of stator core structure were significant, and the effect of viscosity losses on generating developed pressure in the high-slip operations of ALIP can be neglected when compared with the electromagnetic driving force in [20].

The above theoretical research indicated that the equivalent circuit model can quickly reflect the influence of basic parameters on the performance of ALIP, which is of great significance in guiding the design process of ALIP. Besides, the influence of end effects on the developed pressure characteristic of ALIP cannot be eliminated and should be fully taken into account, especially for ALIP with a small pole number. However, the equivalent circuit model proposed previously more considers the role of the fundamental magnetic field, and less or simpler considers the influence of the end effect on the electromagnetic pressure of ALIP. According to the theory of LIMs, the existence of end effects produced by finite stator core length causes the magnetic field in the electromagnetic coupling region to be divided into three components: the fundamental magnetic field, the forward decaying traveling wave magnetic field and the backward decaying traveling wave magnetic field [21]–[23]. The fundamental wave travels with the synchronous speed, however the forward decaying wave moves along the flow direction of liquid metal at a speed less than the synchronous speed and the backward decaying wave moves in the opposite direction of the liquid metal flow at a speed less than the synchronous speed. This means that when the liquid metal flows at a certain speed, the slip corresponding to different traveling wave magnetic field compositions is different in the conversion of the secondary side impedance in the equivalent circuit model, and it is not accurate to calculate the output power by using a single slip under the fundamental wave magnetic field. Therefore, the end effects should be appropriately addressed in the equivalent circuit model.

This paper employs the air-gap flux density equation to develop an improved equivalent circuit model, which considers the influences of the inlet and outlet end-wave flux waves in the annular channel of ALIP. First, the 1-D physical model of ALIP is described, and the distribution expressions of magnetic and electrical fields are presented. The impact of the end effects on electromagnetic field is analyzed. Second, two equivalent circuit models are developed, and the impedance parameters are solved, then the impedance parameters generated by the end effect are abstracted. Finally, the performance of a small ALIP is calculated by the equivalent circuit models, the results obtained from the proposed equivalent circuit models are compared with measured data to validate the rationality and accuracy of this new model.

II. PHSICAL MODEL OF ALIP

A. THE BASIC STRUCTURE AND PRINCIPLE OF ALIP

Fig. 1 shows the schematic of the general structure and principle of ALIP. The ALIP is generally classified into two parts: the primary and the secondary. The primary includes the stator iron core, winding coils and inner core, and the secondary is composed of the ducts with a narrow annular channel and the liquid metal fluid in the annular channel. The stacking thin silicon iron sheets are usually adopted to fabricate the inner and stator cores. In the stator core slots, the disc windings rolling by the copper band are placed. The duct material is made up of stainless steel of the austenite-series of nonferromagnetic material. The annular channel formed between the fixed inner and outer ducts is filled with liquid metal with higher thermal conductivity and electrical conductivity.

When the symmetric three-phase AC supply is applied to the three-phase windings, a traveling wave magnetic field along the axis of the pipeline is generated. Then, eddy currents are induced in the conductive liquid metal when the alternating radial magnetic field passes through the annular channel, thus the interaction between the radial magnetic field and the circumferential eddy currents produces the axial electromagnetic thrust, which pushes the working fluid forward.

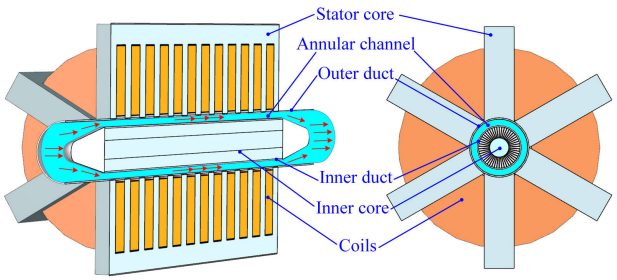

FIGURE 1. Cross section diagram of an ALIP.

B. ONE DIMENSIONAL THEORY MODEL

To solve the magnetic field in the annular channel of ALIP and analyze the influence of end effects on the fundamental characteristics of ALIP, a one-dimensional field model in Cartesian coordinate system is established in Fig. 2. Some assumptions are set as follows for reducing the complexity of calculating [19], [21].

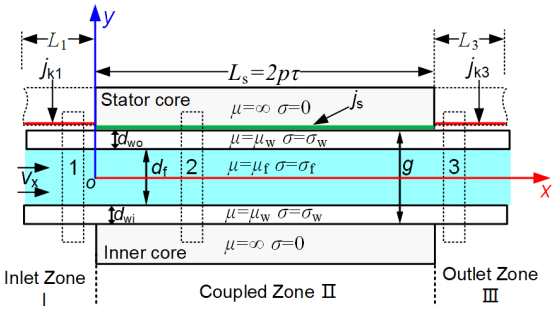

FIGURE 2. Analysis model with the equivalent current sheet of ALIP.

1) The slot effect is equivalent to the Cater coefficient. And the skin effect in the liquid metal flow, core saturation and eddy currents induced in iron core are neglected. The permeability of silicon steel core is infinite, and the conductivity is zero.
2) The input power into a pump is symmetric three phase. All field quantities are sinusoidal functions of time. The magnetic field has only a y component in the non-magnetic gap, and the induced currents are in the z direction.
3) The liquid metal flow is incompressible and considered as a conductive solid with the time-average velocity v_x.

In Fig. 2, a schematic view of the model in the coordinates x and y is presented. The liquid metal flows in from the inlet zone I, through the coupled zone II, out from the zone III along the x-axis through a d_f-width channel between two non-ferromagnetic surfaces. And d_{wi}, d_{wo} are the thickness of the inner and outer ducts respectively, $2p\tau$ is the length of stator iron core, g is the width of the non-magnetic air gap, and $g = d_f + d_{wi} + d_{wo}$. According to the same principle of traveling wave magnetic force [7], [9], the excitation currents of three-phase windings in coupled zone II are equivalent by the line current sheet density j_s without thickness close to the inner surface of the stator core as

$$j_s = \mathrm{Re}\left(J_{s\max} e^{j(\omega t - kx)}\right) \tag{1}$$

where $k = \pi/\tau$, $J_{s\max} = \sqrt{2}(m_1 n_{N1} k_{w1} I_{1pha}/(p\tau))$, ω is the angular velocity, τ is the pole pitch, m_1 is the number of phases, n_{N1} is the number of turns of series-connected primary winding, k_{w1} is the winding coefficient, I_{1pha} is the effective value of applied primary phase current, and p is the number of pole pairs.

In the inlet zone I and the outlet zone III, the fringing fields outside the iron in absence of the conductor can be simulated by assuming that there are proper virtual current sheets (j_{k1}, j_{k3}) [24], which are defined as

$$\left.\begin{aligned} j_{k1} &= -j\sigma_{13} E_{z1} \\ j_{k3} &= -j\sigma_{13} E_{z3} \end{aligned}\right\} \tag{2}$$

where j_{k1} is the virtual current sheet density in region I and j_{k3} is in region III. E_{z1}, E_{z3} represent z-component of the electric field intensity respectively in region I and III. σ_{13} is the virtual conductivity.

C. ANALYSIS APPROCH

The basic equations describing the pumping process in the channel is MHD equations for incompressible flows. And the electromagnetic force, as an external force, which can be described by Maxwell equations. Based the Maxwell equations, introducing the magnetic vector potential $\boldsymbol{A}$ and applying the Ampere's loop theorem to the rectangular loop 1, 2, 3 in the zone I, II, III respectively, three equations about magnetic vector potential are obtained as follows.

$$\frac{g_e}{\mu_0}\frac{d^2A_{11}}{dx^2} - \sigma_f d_f v_f \frac{dA_{11}}{dx} - (j\omega\sigma_f d_f (1 + k_w) - \omega\sigma_{13}) A_{11} = 0 \tag{3}$$

$$\frac{g_e}{\mu_0}\frac{d^2A_{33}}{dx^2} - \sigma_f d_f v_f \frac{dA_{33}}{dx} - (j\omega\sigma_f d_f (1 + k_w) - \omega\sigma_{13}) A_{33} = 0 \tag{4}$$

$$\frac{g_e}{\mu_0}\frac{d^2A_{22}}{dx^2} - \sigma_f d_f v_f \frac{dA_{22}}{dx} - j\omega\sigma_f d_f (1 + k_w) A_{22} = -J_{s\max} e^{-jkx} \tag{5}$$

where

$$k_w = \frac{d_{wi}\sigma_w D_f}{\sigma_f d_f D_{wi}} + \frac{d_{wo}\sigma_w D_f}{\sigma_f d_f D_{wo}} \tag{6}$$

where, A_{11}, A_{22}, A_{33} is the magnetic vector potential function of space in zone I, II and III, separately. k_w shows the effect of stainless-steel ducts, σ_f is the conductivity of liquid metal and σ_w is the conductivity of duct. D_f, D_{wi}, D_{wo} are the average diameter of annular channel, inner and outer ducts, respectively.

According to the distribution function of the theoretical airgap centerline fringing field at the end of an airgap in [25], solving the in Eq. (3) and Eq. (4) under no-load condition

without pipe and liquid metal, then the value of σ_{13} can be represented as

$$\sigma_{13} = -\frac{0.73^2}{g_e \omega \mu_0} = -\frac{k_f^2 g_e}{\omega \mu_0} \tag{7}$$

Then, by solving the Eq. (3)-(5) and combining the relationship between the magnetic vector potential A and the magnetic density B, the expression of the magnetic density in the zone I, II, III is listed in Eq. (8)-(10).

$$B_{y1} = -c_{11} r_{k1} e^{r_{k1} x} e^{j\omega t} \quad x < 0 \tag{8}$$

$$B_{y2} = \left(jkc_t e^{-jkx} - r_1 c_{21} e^{r_1 x} - r_2 c_{22} e^{r_2 x} \right) e^{j\omega t} \quad 0 < x < L_s \tag{9}$$

$$B_{y3} = -c_{12} r_{k3} e^{r_{k3} x} e^{j\omega t} \quad x > L_s \tag{10}$$

where,

$$\begin{aligned} r_{k1} &= \alpha_{k1} + jk\beta_{13}, \quad r_{k3} = \alpha_{k3} - jk\beta_{13} \\ r_{c21} &= \alpha_1 + jk\beta, \quad r_{c22} = \alpha_2 - jk\beta \\ c_t &= \frac{\mu_0 J_{smax}}{k^2 g_e \left(1 + G^2 (s + k_w)^2\right)} - j \frac{\mu_0 J_{smax} G (s + k_w)}{k^2 g_e \left(1 + G^2 (s + k_w)^2\right)} \\ &= c_{t\,Re} + j c_{tm} \end{aligned}$$

where c_{tRe}, c_{tIm} are the real and imaginary parts of c_t. G is the goodness factor. And other parameters are listed in appendix section.

Depending on the continuity of tangent component of magnetic field strength and current at the boundary $x = 0$ and $x = L_s$, the boundary conditions are written as

$$\begin{aligned} B_{y1}\big|_{x=0} &= B_{y2}\big|_{x=0}, \quad B_{y3}\big|_{x=L_s} = B_{y2}\big|_{x=L_s} \\ \frac{\partial B_{y1}}{\mu_0 \partial x}\bigg|_{x=0} &= \frac{\partial B_{y2}}{\mu_0 \partial x}\bigg|_{x=0}, \frac{\partial B_{y3}}{\mu_0 \partial x}\bigg|_{x=L_s} = \frac{\partial B_{y2}}{\mu_0 \partial x}\bigg|_{x=L_s} \end{aligned} \tag{11}$$

Further, from Eq. (11), the four unknown parameters c_{11}, c_{12}, c_{21}, c_{22} are derived and presented in the general complex number form below.

$$\begin{aligned} c_{\substack{i,n \\ i=1,2 \\ n=1,2}} &= c_{\substack{i,nRe \\ i=1,2 \\ n=1,2}} + j c_{\substack{i,nIm \\ i=1,2 \\ n=1,2}} \\ &= \frac{1}{\Gamma_{Re}^2 + \Gamma_{Im}^2} \begin{bmatrix} \Lambda_{Rec_{i,n}} & \Lambda_{Imc_{i,n}} \end{bmatrix} \begin{bmatrix} \Gamma_{Re} & -\Gamma_{Im} \\ \Gamma_{Im} & \Gamma_{Re} \end{bmatrix} \\ &\quad \times \begin{bmatrix} c_{tRe} & c_{tIm} \\ -c_{tIm} & c_{tRe} \end{bmatrix} \begin{bmatrix} 1 \\ j \end{bmatrix} \end{aligned} \tag{12}$$

where $c_{i,nRe}$, $c_{i,nIm}$ are the real and imaginary parts of $c_{i,n}$, the other parameters are given in the appendix section. Besides, defining $|Z|$ as the modulus of complex number Z. And γ_{c11}, γ_{c12}, γ_{c21} and γ_{c22} are defined to satisfy the following formula.

$$\sin \gamma_{\substack{ci,n \\ i=1,2 \\ n=1,2}} = \frac{c_{i,nIm}}{|c_{i,n}|}, \quad \cos \gamma_{\substack{ci,n \\ i=1,2 \\ n=1,2}} = \frac{c_{i,nRe}}{|c_{i,n}|}$$

Furthermore, the explicit complex number expression of the magnetic flux density B in the zone I, II, III can be summarized from Eq. (8)-(10) and Eq. (12).

In the zone II ($0 < x < L_s$)

$$\left.\begin{aligned} B_{y2} &= B_{y2ct} + B_{y2c21} + B_{y2c22} \\ B_{y2ct} &= -k\,|c_t|\, e^{j(\omega t - kx + \arctan(\frac{c_{tIm}}{c_{tRe}}))} \\ B_{y2c21} &= -\,|r_1 c_{21}|\, e^{\alpha_1 x + j(\omega t + k\beta x + \arctan(\frac{k\beta}{\alpha_1}) + \gamma_{c21})} \\ B_{y2c22} &= |r_2 c_{22}|\, e^{\alpha_2 x + j(\omega t - k\beta x + \arctan(\frac{k\beta}{-\alpha_2}) + \gamma_{c22})} \end{aligned}\right\} \tag{13}$$

In the zone I($x < 0$) and zone III ($x > L_s$)

$$B_{y1} = -\,|r_{k1} c_{11}|\, e^{\alpha_{k1} x + j(\omega t + k\beta_{13} x + \arctan(\frac{k\beta_{13}}{\alpha_{k1}}) + \gamma_{c11})} \tag{14}$$

$$B_{y3} = |r_{k3} c_{12}|\, e^{\alpha_{k3}(x - L_s) + j(\omega t - k\beta_{13}(x - L_s) + \arctan(\frac{k\beta_{13}}{-\alpha_{k3}}) + \gamma_{c12})} \tag{15}$$

As shown in Eq. (14)-(15), the magnetic field in both zone I and III are the sinusoidal functions of time which decrease exponentially along the x-axis away from the stator core. Besides, the exponential attenuation factors are determined by α_{k1} and α_{k3}, respectively. Eq. (13) presents that the magnetic field B_{y2} in the coupled zone II contains three components which are B_{y2ct}, B_{y2c21} and B_{y2c22}. B_{y2ct} is the fundamental wave in the constant amplitude which transmits with synchronous speed $2f\tau$. B_{y2c21} and B_{y2c22} are the outlet and inlet end-effect waves, and the wavelength is τ/β. The former is a decaying wave traveling along the x-axis in the negative direction with an attenuation factor of α_1, whereas the latter moves along the x-axis in the positive direction with an attenuation constant of α_2.

The electric field intensity E_{z1}, E_{z2} and E_{z3} in region I, II, III can also be obtained respectively from the magnetic vector potential as follows.

In the zone I($x < 0$) and zone III ($x > L_s$)

$$E_{z1} = \omega\,|c_{11}|\, e^{\alpha_{k1} x + j(\omega t + k\beta_{13} x + \gamma_{c11} + \frac{\pi}{2})} \tag{16}$$

$$E_{z3} = \omega\,|c_{12}|\, e^{\alpha_{k3}(x - L_s) + j(\omega t - k\beta_{13}(x - L_s) + \gamma_{c12} + \frac{\pi}{2})} \tag{17}$$

In the zone II ($0 < x < L_s$)

$$\left.\begin{aligned} E_{z2} &= E_{z2ct} + E_{z2c21} + E_{z2c22} \\ E_{z2ct} &= \omega\,|c_t|\, e^{j(\omega t - kx + \arctan(\frac{c_{tIm}}{c_{tRe}}) + \frac{\pi}{2})} \\ E_{z2c21} &= \omega\,|c_{21}|\, e^{\alpha_1 x + j(\omega t + k\beta x + \gamma_{c21} + \frac{\pi}{2})} \\ E_{z2c22} &= \omega\,|c_{22}|\, e^{\alpha_2 x + j(\omega t - k\beta x + \gamma_{c22} + \frac{\pi}{2})} \end{aligned}\right\} \tag{18}$$

where E_{z2ct}, E_{z2c22} and E_{z2c21} are the electric field intensity from the fundamental magnetic field, the forward and backward traveling magnetic fields.

With Eq. (14)-(18), the induced current in ducts j_{w1}, j_{w2} and j_{w3} are deduced as Eq. (19)-(21).

$$j_{w1} = \omega \sigma_f d_f k_w\,|c_{11}|\, e^{\alpha_{k1} x + j(\omega t + k\beta_{13} x + \gamma_{c11} + \pi/2)} \quad x < 0 \tag{19}$$

$$\left.\begin{aligned} j_{w2} &= j_{w2ct} + j_{w2c21} + j_{w2c22} \\ j_{w2ct} &= \omega \sigma_f d_f k_w\,|c_t|\, e^{j(\omega t - kx + \arctan(\frac{c_{tIm}}{c_{tRe}}) + \frac{\pi}{2})} \\ j_{w2c21} &= \omega \sigma_f d_f k_w\,|c_{21}|\, e^{\alpha_1 x + j(\omega t + k\beta x + \gamma_{c21} + \frac{\pi}{2})} \\ j_{w2c22} &= \omega \sigma_f d_f k_w\,|c_{22}|\, e^{\alpha_2 x + j(\omega t - k\beta x + \gamma_{c22} + \frac{\pi}{2})} \end{aligned}\right\} \quad 0 < x < L_s \tag{20}$$

$$\begin{aligned} j_{w3} &= \omega \sigma_f d_f k_w\,|c_{12}| \\ &\quad \times e^{\alpha_{k3}(x - L_s) + j(\omega t - k\beta_{13}(x - L_s) + \gamma_{c12} + \pi/2)} \quad x > L_s \end{aligned} \tag{21}$$

where j_{w2ct}, j_{w2c22} and j_{w2c21} are the induced current from the fundamental magnetic field, the forward and backward traveling magnetic fields.

Similarly, the induced currents j_{f1}, j_{f2} and j_{f3} in the liquid metal are listed in Eq. (22)-(24).

In the zone I ($x < 0$) and III ($x > L_s$)

$$\begin{aligned} j_{f1} &= -\sigma_f d_f \sqrt{((v_f\alpha_{k1})^2 + (\omega + v_f k\beta_{13})^2)} \\ &\quad \times |c_{11}|\, e^{\alpha_{k1}x} e^{j(\omega t + k\beta_{13}x + \arctan(\frac{\omega + v_f k\beta_{13}}{v_f\alpha_{k1}}) + \gamma_{c11})} \end{aligned} \tag{22}$$

$$\begin{aligned} j_{f3} &= \sigma_f d_f e^{\alpha_{k3}(x-L_s)} \sqrt{((v_f\alpha_{k3})^2 + (v_f k\beta_{13} - \omega)^2)} \\ &\quad \times |c_{12}|\, e^{j(\omega t - k\beta_{13}(x-L_s) + \arctan(\frac{v_f k\beta_{13} - \omega}{-v_f\alpha_{k3}}) + \gamma_{c12})} \end{aligned} \tag{23}$$

In the zone II ($0< x < L_s$)

$$\left.\begin{aligned} j_{f2} &= j_{f2ct} + j_{f2c21} + j_{f2c22} \\ j_{f2ct} &= -js\omega\sigma_f d_f |c_t|\, e^{j(\omega t - kx + \arctan(\frac{c_{tIm}}{c_{tRe}}))} \\ j_{f2c21} &= -\sigma_f d_f e^{\alpha_1 x} \sqrt{((v_f\alpha_1)^2 + (\omega + v_f k\beta)^2)} \\ &\quad \times |c_{21}|\, e^{j(\omega t + k\beta x + \arctan(\frac{\omega + v_f k\beta}{v_f\alpha_1}) + \gamma_{c21})} \\ j_{f2c22} &= \sigma_f d_f e^{\alpha_2 x} \sqrt{((v_f\alpha_2)^2 + (v_f k\beta - \omega)^2)} \\ &\quad \times |c_{22}|\, e^{j(\omega t - k\beta x + \arctan(\frac{v_f k\beta - \omega}{-v_f\alpha_2}) + \gamma_{c22})} \end{aligned}\right\} \tag{24}$$

where j_{f2ct}, j_{f2c22} and j_{f2c21} are the induced current from the fundamental magnetic field, the forward and backward traveling magnetic fields.

From Eq. (18), Eq. (20), Eq. (24), it can be clearly seen that the electric field intensity and induced current in the coupled zone respectively contain three components, which correspond to the fundamental magnetic field, the forward and backward traveling magnetic fields as a consequence of the existence of the end effects.

III. EQUIVALENT CIRCUIT OF ALIP

A. CONVENTIONAL EQUIVALENT CIRCUIT MODEL

Fig. 3 is the conventional equivalent circuit model (EC-I) put forward in [1], [8] and is constantly arranged to estimate the basic performance of ALIP. In Fig. 3, U_1 is the input phase voltage. E_1 is the phase induced electromotive force. I_1, I_m, I_w and I_f are the input phase current, the magnetization current, the total induced current in the ducts and the induced current in the liquid metal respectively. R_1 is the phase resistance of stator winding and X_1 means the leakage reactance of stator winding. X_m represents the magnetization reactance. R_{wo}, R_{wi} are respectively the outer and inner ducts resistance converted into the primary. R_2 is the electrical resistance of liquid metal, and the (1-s)R_2/s stands for the output mechanical power producing the electromagnetic force.

The impedance parameters of the EC-I model are written as follows

$$R_1 = \pi\rho_{cu} n_{N1}(D_{co} + D_{ci})/s_c \tag{25}$$

$$X_1 = 4\mu_0 f \lambda_c \pi^2 n_{N1}^2/(pq) \tag{26}$$

$$X_m = 4m_1\mu_0 f \tau D_{si} k_{w1}^2 n_{N1}^2/(pg_e) \tag{27}$$

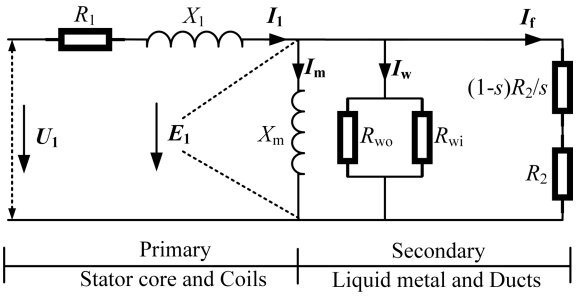

FIGURE 3. The conventional equivalent circuit model of ALIP (EC-I).

$$R_w = \frac{R_{wo}R_{wi}}{R_{wo} + R_{wi}} = \frac{2m_1\pi D_f k_{w1}^2 n_{N1}^2}{\tau p \sigma_f d_f k_w} \tag{28}$$

$$R_2 = 2m_1\pi D_f k_{w1}^2 n_{N1}^2/(\tau p \sigma_f d_f) \tag{29}$$

where D_{ci}, D_{co} are respectively the inner and outer diameters of the winding coil. s_c is the cross-sectional area of a single turn coil. ρ_{cu} is the resistivity of copper winding. λ_c reflects the sum of slot leakage reactance, harmonic leakage reactance and tooth leakage reactance, and the detailed derivation of λ_c is given in the appendix.

The EC-I is developed with only considering the fundamental wave magnetic field. The influence of end effects is not shown in the EC-I model. Although a correcting coefficient (2p-1)/(2p+1) is introduced, which is more suitable for the ALIP with a large pole number, and the accuracy is low for the case with small number of poles.

B. IMPROVED EQUIVALENT CIRCUIT MODEL

In order for the end effects to be reflected in the basic parameters of the equivalent circuit model, this paper proposed the improved equivalent circuit models EC-II (Fig. 4) and EC-III (Fig. 5) based on the established one-dimensional field model in section II.

In EC-II model, K_x, K_{rw}, K_{rf} are respectively correction coefficients of end effects of magnetization reactance, ducts resistance and liquid metal resistance. In EC-III model, K_x, K_{rw} are the same to the Fig. 4. And E_{f1}, E_{f3}, and E_{f2} are the induced electromotive force matched with the forward and backward and fundamental waves, and the sum of them is E_1. $Z_{n,i}$ is the impedance highlighted the interaction of the forward and backward and fundamental waves and it is composed of three components: the resistance $R_{vn,i}$ represents the mechanical power, the resistance $R_{\Delta n,i}$ generating the thermal power and the reactance $X_{n,i}$ producing reactive power. R_f' is the total resistance of the liquid metal. Z_1' and Z'_3 is the impedances introduced by the backward and forward wave. Z'_2 includes the impedance Z_{22} originating from the fundamental wave and the impedances (Z_{21} and Z_{23}) generated by the interaction of backward and forward travelling waves.

The difference between EC-II model and EC-III model is that the former only considers the end effect and still uses the slip of the fundamental wave to separate the output mechanical power and ignores the characteristic that the wavelength of the forward and backward traveling wave is

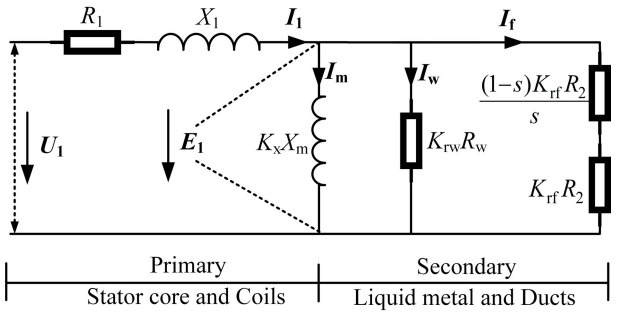

FIGURE 4. The improved equivalent circuit model II (EC-II).

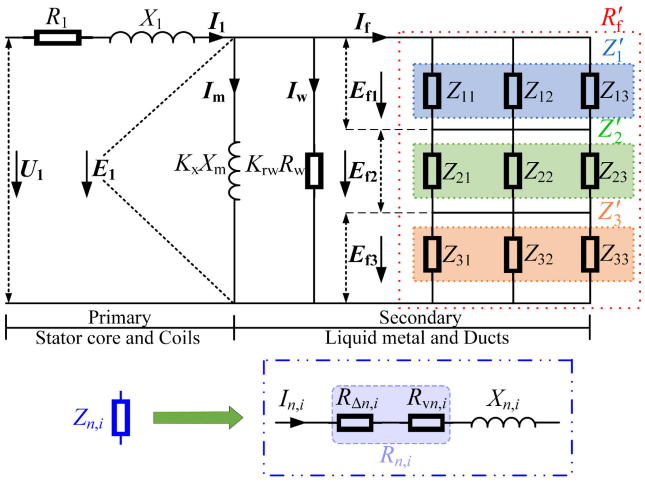

FIGURE 5. The improved equivalent circuit model III (EC-III).

different from the fundamental wave, however in the latter, the issues are taken into full account and the output powers corresponding to the forward traveling wave, backward traveling wave and the fundamental wave are extracted as separate impedance parameters. Considering the output powers of the zone I and III in Fig. 2 are far less than that of the coupled zone II because of the rapid decay of the magnetic fields, especially in the large slip, and the conventional slip of ALIP is greater than 0.3, therefore, to simplify the calculation, this paper ignores the power in the zone I and III when calculating the equivalent circuit parameters in EC-II and EC-III models.

Based on the equal complex power relationship between the magnetic field and the electrical circuit, the parameters in EC-II and EC-III models can be calculated by the electromagnetic parameters obtained from the one-dimensional field model. Stator phase resistance R_1 and stator winding leakage reactance X_1 is independent to the end effects, so they are same to EC-I model. The other parameters are derived as follows.

1) THE INDUCED ELECTROMOTIVE FORCE

According to the Eq. (1) and Eq. (18), the total input power S_{i2} from the primary is obtained as

$$S_{i2} = \frac{\pi D_{si}}{2}\int_0^{L_s} -j_s^* E_{z2}\,dx = P_{i2} + jQ_{i2} \tag{30}$$

where j_s^* means the conjugate of j_s. The active power P_{i2} and the reactive power Q_{i2} are written as

$$P_{i2} = \frac{\pi\omega\mu_0 D_{si}L_s G\,(s+k_w)\,J_{smax}^2}{2k^2 g_e\left(1+G^2\,(s+k_w)^2\right)}C_p \tag{31}$$

$$Q_{i2} = \frac{\pi\omega\mu_0 D_{si}L_s G\,(s+k_w)\,J_{smax}^2}{2k^2 g_e\left(1+G^2\,(s+k_w)^2\right)}C_q \tag{32}$$

where C_p and C_q are presented in the appendix section.

Then the phase induced electromotive force E_1 is derived as

$$E_1 = \frac{S_{i2}}{m_1 I_1} = \frac{\sqrt{2}\pi\omega\mu_0 n_{N1}k_{w1}D_{si}GJ_{smax}\,(s+k_w)\left(C_p + jC_q\right)}{k^2 g_e\left(1+G^2\,(s+k_w)^2\right)} \tag{33}$$

2) THE MAGNETIZATION REACTANCE

The magnetization reactance $X'_m(X'_m = K_xX_m)$ with end effects can be calculated by the relationship of Q_{i2} and E_1.

$$X'_m = \frac{m_1\,|E_1|^2}{Q_{i2}} = \frac{G\,(s+k_w)}{1+G^2\,(s+k_w)^2}\frac{C_p^2+C_q^2}{C_q}X_m \tag{34}$$

where X_m is the magnetization reactance with no end effects.

The correction factor K_x of end effect of magnetization reactance is presented as follow

$$K_x = \frac{G\,(s+k_w)\left(C_p^2+C_q^2\right)}{C_q\left(1+G^2\,(s+k_w)^2\right)} \tag{35}$$

Then the magnetizing current I_m is solved.

$$I_m = \left(\frac{jQ_{i2}}{m_1E_1}\right)^* = \frac{p\tau J_{smax}C_q\left(C_q - jC_p\right)}{\sqrt{2}m_1n_{N1}k_{w1}\left(C_p^2+C_q^2\right)} \tag{36}$$

3) THE DUCTS RESISTANCE

The power consumed on ducts S_{w2} can be given by Eq. (18) and Eq. (20).

$$\begin{aligned} S_{w2} = P_{w2} &= \frac{\pi D_f}{2}\int_0^{L_s} j_{w2}^* E_{z2}\,dx \\ &= \frac{\pi\omega^2 D_f\sigma_f d_f k_w L_s\mu_0 J_{smax}G\,(s+k_w)}{2k^2 g_e\left(1+G^2\,(s+k_w)^2\right)}C_w \end{aligned} \tag{37}$$

where the coefficient C_w are listed in the appendix section. Since the secondary leakage reactance is ignored in the 1-D model, the imaginary part of S_{w2} is zero and the active power P_{w2} belongs to thermal power.

The total resistance R'_w ($R'_{rw} = K_{rw}R_w$) of the inner and outer ducts are deduced with P_{w2} and E_1.

$$R'_w = \frac{m_1\,|E_1|^2}{P_{w2}} = \frac{\mu_0 J_{smax}D_{si}^2 G\,(s+k_w)\left(C_p^2+C_q^2\right)}{g_e k^2 D_f^2 C_w\left(1+G^2\,(s+k_w)^2\right)}R_w \tag{38}$$

Thus, the correction factor K_{rw} of end effect of duct resistance is

$$K_{rw} = \frac{\mu_0 J_{smax}D_{si}^2 G\,(s+k_w)\left(C_p^2+C_q^2\right)}{g_e k^2 D_f^2 C_w\left(1+G^2\,(s+k_w)^2\right)} \tag{39}$$

And the induced current I_w in the ducts is also obtained as below.

$$I_w = \left(\frac{S_{w2}}{m_1 E_1}\right)^* = \frac{\omega p \tau \sigma_f d_f k_w C_w \left(C_p + jC_q\right)}{\sqrt{2} m_1 n_{N1} k_{w1} \left(C_p^2 + C_q^2\right)} \quad (40)$$

4) THE LIQUID METAL RESISTANCE

With the obtained powers and the currents in the two branches-magnetization reactance and ducts resistance, the power consumed in the liquid metal P_{f2} and the induced current I_f in it are computed in Eq. (41)-(42).

$$\begin{aligned} P_{f2} &= P_{i2} - P_{w2} \\ &= \frac{G(s + k_w)}{2k^2 g_e \left(1 + G^2 (s + k_w)^2\right)} \\ &\quad \times \pi \omega \mu_0 L_s J_{smax} \left(D_{si} J_{smax} C_p - \omega D_f \sigma_f d_f k_w C_w\right) \end{aligned} \quad (41)$$

$$\begin{aligned} I_f &= I_1 - I_m - I_w \\ &= \frac{p\tau \left(C_p + jC_q\right) \left(J_{smax} C_p - \omega \sigma_f d_f k_w C_w\right)}{\sqrt{2}\, m_1 n_{N1} k_{w1} \left(C_p^2 + C_q^2\right)} \end{aligned} \quad (42)$$

So, the resistance R'_f ($R'_f = K_{rf} R_2/s$) of the liquid metal and the correction factor K_{rf} of end effect are described as

$$\begin{aligned} R'_f &= \frac{E_1}{I_f} \\ &= \frac{2\mu_0 f \sigma_f d_f \tau^2 D_{si} J_{smax} G(s + k_w)(C_p^2 + C_q^2) R_2}{\pi g_e D_f \left(1 + G^2 (s + k_w)^2\right) \left(C_p J_{smax} - \omega \sigma_f d_f k_w C_w\right)} \end{aligned} \quad (43)$$

$$K_{rf} = \frac{2\mu_0 s f \sigma_f d_f \tau^2 D_{si} J_{smax} G(s + k_w)(C_p^2 + C_q^2)}{\pi g_e D_f \left(1 + G^2 (s + k_w)^2\right) \left(C_p J_{smax} - \omega \sigma_f d_f k_w C_w\right)} \quad (44)$$

To further extract the impedance parameters corresponding to the forward and backward traveling wave magnetic fields in EC-III model, the power S_{f2} consumed in the liquid metal is computed by j_{f2} and E_{z2}.

$$\begin{aligned} S_{f2} &= P_{f2} = \frac{\pi D_f}{2} \int_0^{L_s} j_{f2}^* E_{z2} dx \\ &= \frac{\pi D_f}{2} \int_0^{L_s} \left(\begin{array}{l} \left(j_{f2c21}^* + j_{f2ct}^* + j_{f2c22}^*\right) \\ \times \left(E_{z2c21} + E_{z2ct} + E_{z2c22}\right) \end{array} \right) dx \end{aligned} \quad (45)$$

For the sake of formal uniformity, the following definitions are introduced.

$$\left.\begin{array}{l} S_{f2} = \sum\limits_{n,i=1}^{3} S_{fn,i},\ S_{fn,i} = P_{fn,i} + jQ_{fn,i} \\ \sum\limits_{n,i=1}^{3} Q_{fn,i} = 0,\ P_{f2} = \sum\limits_{n,i=1}^{3} P_{fn,i} \qquad n, i = 1, 2, 3 \\ E_1 = \sum\limits_{n=1}^{3} E_{fn},\ E_{fn} = \left(\sum\limits_{i=1}^{3} S_{fn,i}\right) / \left(m_1 I_f^*\right) \end{array}\right\}$$

The matrix form of the power $S_{fn,i}$ in each branch in EC-III model is presented as

$$\underset{\substack{n=1,2,3 \\ i=1,2,3}}{S_{fn,i}} = \frac{\pi D_f}{2} \int_0^{L_s} \begin{bmatrix} j_{f2c21}^* E_{z2c21} & j_{f2ct}^* E_{z2c21} & j_{f2c21}^* E_{z2ct} \\ j_{f2c21}^* E_{z2c22} & j_{f2ct}^* E_{z2ct} & j_{f2c22}^* E_{z2c21} \\ j_{f2c22}^* E_{z2ct} & j_{f2ct}^* E_{z2c22} & j_{f2c22}^* E_{z2c22} \end{bmatrix} dx \quad (46)$$

Then the impedance $Z_{n,i}$ of each branch, Z'_1 introduced by the backward and Z'_3 introduced by the forward wave are derived as the following forms.

$$\left.\begin{array}{l} Z_{n,i} = \dfrac{m_1 |E_{fn}|^2}{S_{fn,i}^*} = R_{n,i} + jX_{n,i} \\ Z'_n = 1/\left(1/Z_{n1} + 1/Z_{n2} + 1/Z_{n3}\right) \end{array} \quad n, i = 1, 2, 3 \right\} \quad (47)$$

where $R_{n,i}$ is sum of the thermal power resistance $R_{\Delta n,i}$ and the mechanical power resistance $R_{vn,i}$.

To avoid the error caused by the difference of the wavelength of the forward, backward and fundamental traveling waves, the output mechanical power P_{f2v} for propelling the flow of liquid metal is produced by Eq. (13) and Eq. (24).

$$\begin{aligned} P_{f2v} &= \frac{\pi v D_f}{2} \int_0^{L_s} -\mathrm{Re}\left(j_{f2}^* B_{y2}\right) dx \\ &= \frac{-\pi v D_f}{2} \int_0^{L_s} \mathrm{Re}\left(\begin{array}{l} \left(j_{f2c21}^* + j_{f2ct}^* + j_{f2c22}^*\right) \\ \times \left(B_{y2c21} + B_{y2ct} + B_{y2c22}\right) \end{array} \right) dx \end{aligned} \quad (48)$$

With Eq. (48), the mechanical power $P_{vn,i}$ in each branch in EC-III model is also obtained. Analogously, the matrix form of it is exhibited as

$$\begin{aligned} &\underset{\substack{n=1,2,3 \\ i=1,2,3}}{P_{vn,i}} \\ &= \frac{-\pi v D_f}{2} \int_0^{L_s} \begin{bmatrix} j_{f2c21}^* B_{z2c21} & j_{f2ct}^* B_{z2c21} & j_{f2c21}^* B_{z2ct} \\ j_{f2c21}^* B_{z2c22} & j_{f2ct}^* B_{z2ct} & j_{f2c22}^* B_{z2c21} \\ j_{f2c22}^* B_{z2ct} & j_{f2ct}^* B_{z2c22} & j_{f2c22}^* B_{z2c22} \end{bmatrix} dx \end{aligned} \quad (49)$$

Moreover, the mechanical power resistance $R_{vn,i}$ and the thermal power resistance $R_{\Delta n,I}$ of each branch are shown as follows.

$$\left.\begin{array}{l} R_{vn,i} = P_{vn,i} R_{n,i} / P_{fn,i} \\ R_{\Delta n,i} = \dfrac{\left(P_{fn,i} - P_{vn,i}\right) R_{n,i}}{P_{fn,i}} \end{array} \quad n, i = 1, 2, 3 \right\} \quad (50)$$

5) THE DEVELOPED PRESSURE

For the hydraulic pressure losses [10], Darcy-Weisbach Formula is adopted for calculating major hydraulic loss ΔP_M caused by friction between the duct and fluid in the annular channel of ALIP in Eq. (51). Moreover, minor losses ΔP_m occurring at both ends of the flow gap are calculated in Eq. (52).

$$\Delta P_M = f_d \rho_f L v_f^2 / (2D_h) \quad (51)$$

$$\Delta P_m = K_m \rho_f v_r^2 / 2 \quad (52)$$

where, L is the length of the annular channel of ALIP, D_h is the Hydraulic diameter of the flow channel, f_d is Darcy friction factor, K_m is minor loss coefficient, v_r is the velocity in the torpedo reducer.

Finally, with the expressions of hydraulic loss and the parameters obtained in EC-I, II and III models, the developed pressures of ALIP in different equivalent circuits are given as follows.

The developed pressure with EC-I model [12], [26]

$$\Delta P_d^I = \frac{36sf\sigma_f\mu_0^2\tau^2(n_{N1}k_{w1}I_1)^2}{p\left(\pi^2 g_e^2+\left(2\mu_0 f\sigma_f d_f\tau^2\,(s+k_w)\right)^2\right)} - \Delta P_M - \Delta P_m \tag{53}$$

The developed pressure with EC-II model

$$\Delta P_d^{II} = \frac{s\,(1-s)\,m_1 I_1^2}{v\pi D_f d_f K_{rf} R_2\left|\frac{s}{K_{rf}R_2}+\frac{1}{K_{rw}R_w}+\frac{1}{jK_xX_m}\right|^2} - \Delta P_M - \Delta P_m \tag{54}$$

The developed pressure with EC-III model

$$\Delta P_d^{III} = \frac{m_1 I_1^2 \sum_{n=1;i=1}^{3}\left(R_{vn,i}\left|Z_n'\right|^2/\left|Z_{n,i}\right|^2\right)}{v\pi D_f d_f R_f'^2\left|\frac{1}{R_f'}+\frac{1}{K_{rw}R_w}+\frac{1}{jK_xX_m}\right|^2} - \Delta P_M - \Delta P_m \tag{55}$$

IV. RESULTS AND DISCUSSION

In this section, a small three-phase ALIP is designed, and the design parameters and material properties are shown in Table 1.

Based on this ALIP, the distribution of electromagnetic field and the influence of end effects on it are analyzed by using the formula deduced above. The developed pressures of ALIP with EC-I, II and III models are compared.

A. THE DISTRIBUTION OF MAGNETIC FIELD

Fig. 6 is draw by Eq. (14)-(13) with the load condition of $I_{line} = 44A$, $f = 50Hz$, $v_f = 3m/s$. Fig. 6(a) illustrates the space-time distribution of the synthetic magnetic field in the annular channel of the designed ALIP. And the magnitude of it along the axial direction is arranged as Fig. 6(b). Fig. 6(c) describes the axial amplitude distribution of all magnetic field components including the fundamental traveling wave magnetic field B_{y2ct}, the forward B_{y2c22} and backward B_{y2c21} traveling wave magnetic fields with different slips in the coupled zone. The comparison figure of the attenuation factors of different decaying magnetic fields (B_{y2c21}, B_{y2c22}, B_{y1} and B_{y3}) versus flow rate with different frequency is presented in Fig. 6(d).

With Fig. 6(a), it is observed that the magnetic fields in zones I, II and III are all sinusoidal functions of time, and in space. In Fig. 6(b) and Fig. 6(c), because of the end effects, the magnetic field B_{y2} in coupled zone II is composed of three magnetic field components, which are the fundamental magnetic field B_{y2ct} moving along the flow direction with a speed of $2f\tau$, the attenuated forward traveling magnetic field B_{y2c22} with a speed $2f\tau/\beta$ and the attenuated backward B_{y2c21} traveling magnetic field with a speed $-2f\tau/\beta$.

For B_{y2ct}, the magnitude of it is constant independent of time and location and increases gradually with the decrease of slip. However, B_{y2c22} and B_{y2c21} start to decay from the inlet and outlet of the coupled zone along the axial direction with attenuation coefficients α_2 and α_1 respectively. In Fig. 6(c) and Fig. 6(d), it can be seen that α_1 is equal to $-\alpha_2$ and the corresponding attenuation distance and the magnetic field amplitude at the end of them are same when $s = 1$. When $s < 1$, the attenuation factor α_1 of B_{y2c21} increases and the attenuation distance and the magnetic field amplitude at the end decreases with the increase of flow rate at the condition of constant frequency, and yet the regularity of attenuation factor $-\alpha_2$ and attenuation distance of B_{y2c22} are opposite and the characteristic of magnetic field amplitude at the end is the same. When the flow rate is constant, the attenuation factors both increases with the increase of frequency. In addition, the attenuation distance of B_{y2c22} is more sensitive to the variation of slip, and the amplitude of B_{y2c21} at the end is greatly affected by the slip. When the slip is large, the effects of both cannot be ignored compared with the fundamental wave B_{y2ct}.

In Fig. 6(a) and Fig. 6(b), the magnetic field B_{y1} and B_{y3} decay faster in the opposite direction along axial annular channel, respectively. The amplitude of B_{y1} at location of $x = 0$ is smaller than B_{y3} at $x = L_s$ as result of the distortion of B_{y2}. The attenuation factor α_{k1} increases as flow rate increases, as $-\alpha_{k3}$, by contrast, decreases gradually. Moreover, different from α_1 and α_2, α_{k1} and α_{k3} is independent of frequency. Since the attenuation trend of the magnetic fields

TABLE 1. The main parameters of Alip.

Symbol		Quantity	Unit	Values
Basic Parameters	T	Operating Temperature	°C	75
	p	Number of poles		2
	m	Number of phases		3
	N_s	Number of slots		12
	τ	Pole pitch	mm	170
	L_s	Stator core length	mm	340
	D_f	Annular channel diameter	mm	38
	d_f	Annular channel width	mm	6
	d_{wo}	Outer duct thickness	mm	1
	d_{wi}	Inner duct thickness	mm	1
Liquid Metal Ga (75°C)	T_M	Melt Temperature	°C	29.76
	ρ_f	Mass density	m^3/kg	6083
	σ_f	Electrical conductivity	S/m	3.8×10^6
	μ_r	Relative permeability		1
	η	Absolute viscosity	mPa·s	1.809
Stainless-steel ducts (SUS 316)	σ_w	Conductivity	S/m	1.2×10^6
	μ_r	Relative permeability		1

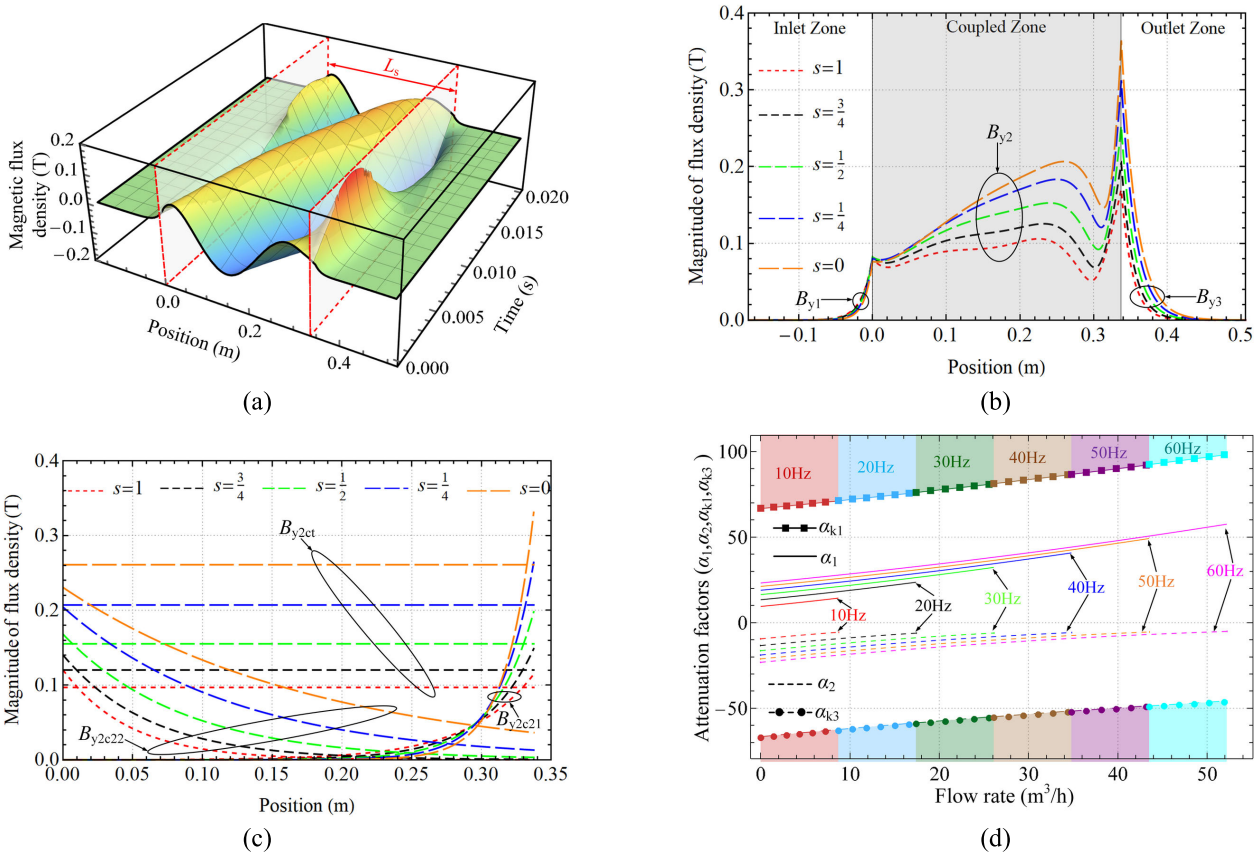

FIGURE 6. The magnetic field distribution in annular channel of ALIP. (a) The temporal and spatial distribution of synthetic magnetic field. (b) The axial distribution of the magnitude of flux density in zone I, II and III. (c) The axial distribution of the amplitude of different magnetic field components in coupled zone II. (d) The attenuation factors of different decaying magnetic fields (B_{y2c21}, B_{y2c22}, B_{y1} and B_{y3}) versus flow rate with different frequency.

(B_{y1} and B_{y3}) are in accord with exponential function, meanwhile, α_{k1} and -α_{k3} are much bigger than α_1 and -α_2 respectively, the contributions of B_{y1} and B_{y3} are negligible to a certain extent, especially with large slip.

Compared with B_{y2ct}, the backward wave B_{y2c2} enhances the effect of the fundamental magnetic field and the forward wave B_{y2c1} weakens it at the ends of coupled zone. The end effects cause the distortion of the synthetic magnetic field B_{y2}, and the distortion becomes more serious with the increase of flow velocity.

B. THE CORRECTION FACTOR OF THE END EFFECT OF IMPEDANCE

Based on three equivalent circuits that have been solved, Fig. 7 and Fig. 8 are illustrated in bellow.

Fig. 7 (a)-(c) show respectively the variation trends of end effect correction coefficients (K_x, K_{rw} and K_{rf}) of the magnetizing reactance, duct resistance and liquid metal resistance with flow velocity at different frequencies. Fig. 7(d) presents the variation characteristics of K_{rf}/s relative to the flow rate with different frequencies.

In Fig. 7(a), $K_x = 1$ means that there are no end effects. When the frequency is less than 30Hz, K_x is greater than 1, and the end effects enhance the magnetizing reactance. On the other hand, K_x is less than 1 when the frequency is greater than 30Hz, namely the magnetizing reactance is weakened by end effects. In addition, when the flow rate is zero, the value of K_x decreases gradually with the increase of frequency and approaches a stable value. For the flow rate, at 10Hz, K_x slowly increases with the increase of flow rate, and the increase is very small, while it decreases step by step at frequency not less than 20Hz.

Similarly, K_{rw} is equal to 1 without considering end effects in Fig. 7(b). At all frequencies, K_{rw} decreases with increasing flow velocity. When the frequency is 10Hz, K_x is less than 1, and the end effects reduce the duct resistance. As the increase of frequency, at 20Hz, $K_{rw} > 1$ when the slip is less than 0.5, on the contrary, $K_{rw} < 1$. Then, K_{rw} is greater 1 when frequency is no less than 30Hz. Finally, K_{rw} reaches a stable value greater than 1 at a certain frequency.

According to the results of Fig. 7(c), it can be obtained that K_{rf} is bigger than 1 when slip is large at the range of 30Hz-60Hz. At 10Hz-20Hz, K_{rf} is smaller than 1. Moreover, the K_{rf} has a similar pattern to K_{rw} as the velocity or frequency increases. In Fig. 7(d), it is obviously that K_{rf}/s does not reach the infinity at the synchronous flow rate of the

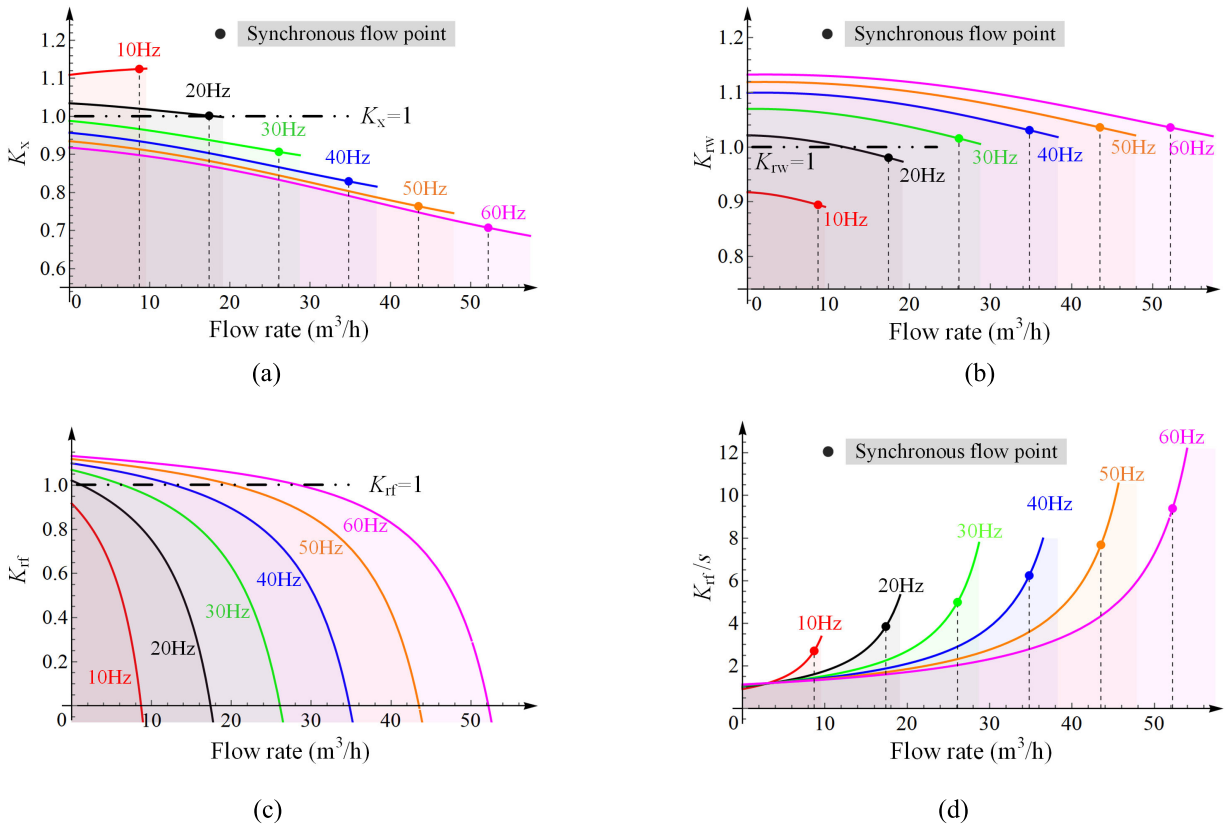

FIGURE 7. The End-effects correction coefficients for magnetizing reactance (a), duct resistance (b) and liquid metal resistance (c)-(d) versus the flow rate with different frequencies.

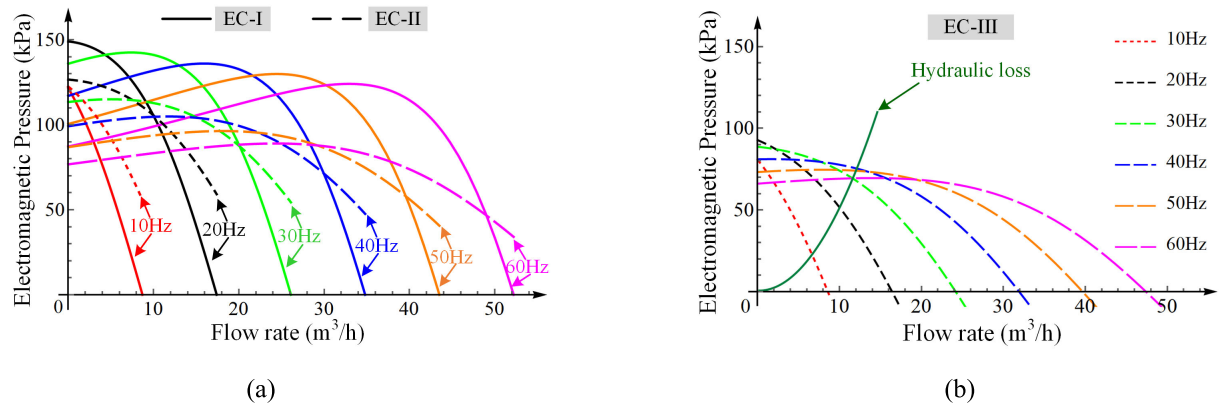

FIGURE 8. The electromagnetic pressure versus flow rate at different frequencies for EC-I, EC-II (a), and EC-III (b).

fundamental travelling wave magnetic field, in other words, the forward and backward traveling wave magnetic fields produced by the end effects causes the slip is the mixture of some slips. Therefore, it is imprecise to calculate the output mechanical power by using a single slip from the fundamental wave.

However, one thing needs to be mentioned that the curve of K_{rf} or K_{rf}/s changes gently with the flow velocity at large slip and high frequency, which means that the slip has little influence on them. Since the end effects are taken into account and the operating slip of ALIP is large, this method computing the mechanical power by the fundamental wave slip can be used for performance prediction of ALIP at some level, which (EC-II) is more reliable than the case (EC-I) where the end effect is not taken into account. Of course, the most accurate approach to obtain the impedance parameters of the liquid metal through the 1-D field model to avoid the introduction of slip, such as EC-III.

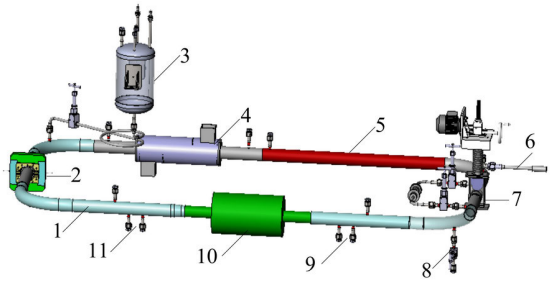

1-The Loop Pipe, 2-Electromagnetic Flow Meter, 3-Expansion Tank, 4-Cold Trap, 5-The Heater, 6-Explosion-Proof Heating Rod, 7-Flow Control Valve, 8-Fill-Discharge Valve, 9-Inlet Pressure Transducer, 10-ALIP, 11-Outlet Pressure Transducer

(a)

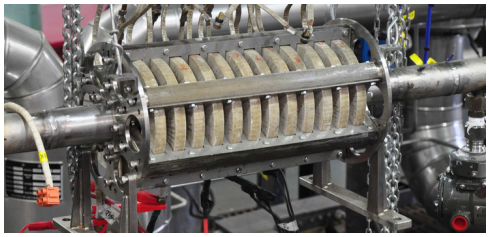

(b)

FIGURE 9. 3D schematic diagram of test loop (a) of the fabricated ALIP (b) for experiment.

C. THE ELECTROMAGNETIC PRESSURE WITH DIRRERENT EC MODELS

Under the premise of introducing no fluid loss, the electromagnetic pressures from EC-I, EC-II and EC-III models with different frequencies are shown in Fig. 8.

With Fig. 8(a), comparing the results of EC-I and EC-II models, it can be inferred that the electromagnetic pressure calculated by the latter is higher than that of the former in the whole range of synchronous flow velocity at 10Hz. With the increase of frequency, the electromagnetic pressure of the latter is smaller than that of the former in a certain range of flow rate, and the flow rate range that meets the requirement is also getting wider and wider. This means that the accuracy of EC-II model is better than EC-I model gradually with the increase of frequency in a large slip range.

Fig. 8(b) reveals the electromagnetic pressure with EC-III model in different frequencies and the curve (solid line) of hydraulic loss versus the flow rate. Compared with EC-I and EC-II models, this model eliminates the error of the slip in EC-II model and considers the end effects, so the results gained are smaller and accurate, meanwhile, it also shows that the end effects cannot be ignored. Moreover, since hydraulic loss increases rapidly with the increase of the flow rate, which greatly limits the operating range of ALIP, and the maximum flow rate is much smaller than the synchronized flow velocity. Finally, with the hydraulic loss, the developed pressures from the equivalent circuit models are draw in Fig. 10 at different frequencies.

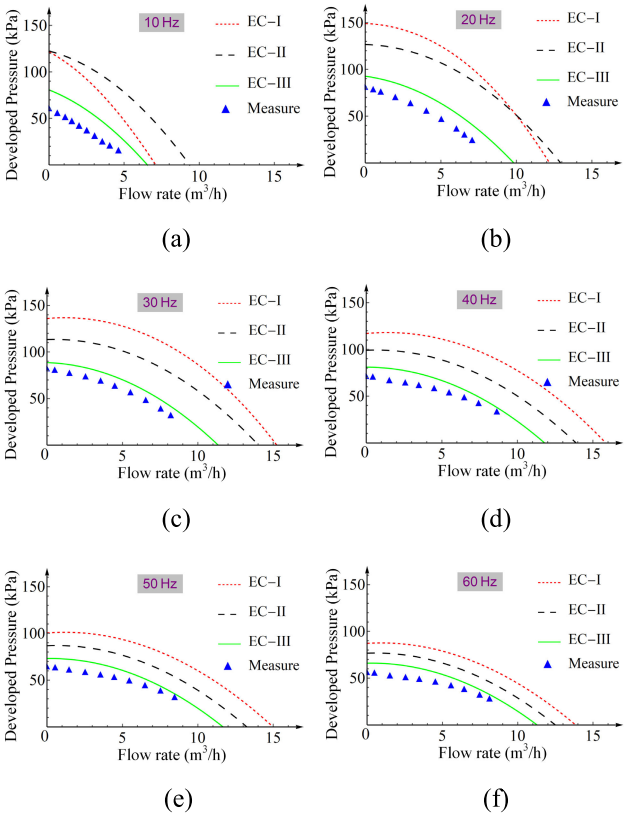

FIGURE 10. Comparison curves of calculated and measured developed pressures under different frequencies and constant current.

V. EXPERIMENTAL TEST

Based on the analysis results of the equivalent circuit models and the design parameters in Table 1, the electromagnetic field distribution and impedance parameters in EC-I, EC-II and EC-III are presented. And the electromagnetic pressures and developed pressures of the designed ALIP with the three equivalent circuits model at different frequencies are compared. In order to verify the rationality and accuracy of the proposed equivalent circuit models based on the 1-D field model, a small ALIP is manufactured and the ALIP experimental test loop is constructed. The 3D schematic of this loop and the test ALIP are displayed in Fig. 9. Based on the test circuit, the developed pressures at different frequencies are tested, and the measured results are compared with the calculated values from EC-I, EC-II and EC-III, as shown in Fig. 10.

With the analysis results from Fig. 10, it can be acquired that the variation trend of the calculated results of the three equivalent circuit models are basically consistent with the experimental values. The calculation results of EC-III model are closer to the experimental values (average error 13%), and EC-II model is not far behind except 10Hz, then EC-I model is the worst. Moreover, the calculated values are generally higher than measure data and the large errors mainly occur in the conditions of 10Hz. The error is mainly caused by the

nonlinear saturation effect of ferromagnetic material, especially in low frequency conditions.

VI. CONCLUSION

This paper acquires the analytical formulas of electromagnetic fields in the annular channel of ALIP by building up the 1-D analysis model. Based on this model, the improved equivalent circuit models (EC-II and EC-III) are developed to calculate the performance for ALIP. Meanwhile, the test loop of a small designed ALIP is set up to validate the reliability of proposed models. According to contrastive analysis of the results gained from the conventional equivalent circuit (EC-I), EC-II, EC-III and experimental data, it can be learned that the EC-II model taking end effects into account have the better results than EC-I model without end effects, and the results from EC-III model considering further the difference of synchronous velocity among the end effect traveling waves and the fundamental wave are closer to the experimental values than EC-II model only with end effects. In other words, the end effects are not obviously neglectable when establishing the equivalent circuit model of ALIP. And the difference of synchronous velocity among the end effect traveling waves and the fundamental wave can introduce the error when calculating the resistance which represents the output mechanical power generating the electromagnetic pressure.

Compared with the conventional equivalent circuit (EC-I) the solving accuracy of both EC-II and EC-III models is significantly improved due to taking the influences of the end effects into account. About the EC-II and EC-III models, in contrast, the former is clear in terms of parameters simplicity, and the latter has the higher precision and reliability. In general, the EC-III model considering the end effects and the issue of slip is the optimal.

APPENDIX

The relevant parameters and coefficients not listed in the text are listed in the appendix as follows.

The decaying factor and other parameters of magnetic field B_{y1}, B_{y3}, B_{y2c21} and B_{y2c22}.

$$\begin{aligned}
\alpha_{k1} &= \frac{M}{2}\left(1+\sqrt{\frac{Y+X}{2}}\right), \quad \alpha_{k3} = \frac{M}{2}\left(1-\sqrt{\frac{Y+X}{2}}\right)\\
\alpha_1 &= \frac{1}{2}M + \frac{\sqrt{2}}{4}\sqrt{\sqrt{M^4+N^2}+M^2}\\
\alpha_2 &= \frac{1}{2}M - \frac{\sqrt{2}}{4}\sqrt{\sqrt{M^4+N^2}+M^2}\\
\beta_{13} &= \frac{M}{2k}\sqrt{\frac{Y-X}{2}}, \quad \beta = \frac{\sqrt{2}}{4k}\sqrt{\sqrt{M^4+N^2}-M^2}\\
M &= (1-s)kG, \quad N = 4k^2G\,(1+k_w)\\
X &= 1-\frac{4\sigma_{13}}{\sigma_f d_f G(1-s)^2}, \quad Y = \sqrt{X^2+\frac{16(1+k_w)^2}{G^2(1-s)^4}}\\
G &= 2f\,\mu_0\sigma_f d_f \tau^2/(\pi g_e)
\end{aligned} \tag{56}$$

The leakage coefficient λ_c of stator is

$$\lambda_c = 4\pi^2\mu_0 f\frac{n_{N1}^2}{pq}\left(\begin{array}{l}(D_{co}+D_{ci})\left(\frac{D_{co}-D_{ci}}{6w_s}+\frac{D_{ci}-D_{si}}{2w_s}\right)\\ +\frac{mq\tau D_{si}}{\pi^2 g_e}\sum\limits_{\substack{v=-\infty\\ v\neq 1}}^{v=+\infty}\left(\frac{k_{wv}}{v}\right)^2 + D_{si}\frac{5g}{5w_s+4g}\end{array}\right) \tag{57}$$

The parameters in the expressions of $c_{i,nRe}$ and $c_{i,nIm}$ is listed in Eq. (58)-(62).

$$\left.\begin{aligned}
\Lambda_{Rec_{11}} &= -2\pi k\beta\,(\beta_{13}-1)+\alpha_{k3}\tau\,(\alpha_2-\alpha_1)\\
&\quad+\sqrt{\xi_{\Lambda c_{11}}^2+\lambda_{\Lambda c_{11}}^2}\,e^{\alpha_1 L_5}\sin\left(\beta k L_s+\theta_{\Lambda c_{11}}\right)\\
&\quad+\sqrt{\xi_{11}'^2+\lambda_{\Lambda c_{11}}'^2}\,e^{\alpha_2 L_3}\sin\left(\beta k L_s+\theta'_{\Lambda c_{11}}\right)\\
\Lambda_{Imc_{11}} &= \pi\left((\alpha_2-\alpha_1)(1-\beta_{13})-2\alpha_{k3}\beta\right)\\
&\quad-\sqrt{\xi_{\Lambda c_{11}}^2+\lambda_{\Lambda c_{11}}^2}\,e^{\alpha_1 L_3}\cos\left(\beta k L_s+\theta_{\Lambda c_{11}}\right)\\
&\quad+\sqrt{\xi_{\Lambda c_{11}}'^2+\lambda_{\Lambda c_{11}}'^2}\,e^{\alpha_2 L_5}\cos\left(\beta k L_s+\theta'_{\Lambda c_{11}}\right)
\end{aligned}\right\} \tag{58}$$

$$\left.\begin{aligned}
\Lambda_{Rec_{12}} &= e^{(\alpha_1+\alpha_2)L_s}\left(-2\pi k\beta\,(\beta_{13}+1)-\alpha_{k1}\tau\,(\alpha_2-\alpha_1)\right)\\
&\quad+\sqrt{\xi_{\Lambda c_{12}}^2+\lambda_{\Lambda c_{12}}^2}\,e^{\alpha_1 L_s}\sin\left(\beta k L_s+\theta_{\Lambda c_{12}}\right)\\
&\quad+\sqrt{\xi_{\Lambda c_{12}}'^2+\lambda_{\Lambda c_{12}}'^2}\,e^{\alpha_2 L_s}\sin\left(\beta k L_s+\theta'_{\Lambda c_{12}}\right)\\
\Lambda_{Imc_{12}} &= \pi e^{(\alpha_1+\alpha_2)L_s}\left((\alpha_1-\alpha_2)(1+\beta_{13})+2\alpha_{k1}\beta\right)\\
&\quad-\sqrt{\xi_{\Lambda c_{12}}^2+\lambda_{\Lambda c_{12}}^2}\,e^{\alpha_1 L_s}\cos\left(\beta k L_s+\theta_{\Lambda c_{12}}\right)\\
&\quad+\sqrt{\xi_{\Lambda c_{12}}'^2+\lambda_{\Lambda c_{12}}'^2}\,e^{\alpha_2 L_s}\cos\left(\beta k L_s+\theta'_{\Lambda c_{12}}\right)
\end{aligned}\right\} \tag{59}$$

$$\left.\begin{aligned}
\Lambda_{Rec_{21}} &= -\pi k\,(\beta_{13}-1)(\beta_{13}+\beta)-\alpha_{k3}\tau\,(\alpha_{k1}-\alpha_2)\\
&\quad+\sqrt{\xi_{\Lambda c_{21}}^2+\lambda_{\Lambda c_{21}}^2}\,e^{\alpha_2 L_3}\sin\left(\beta k L_s+\theta_{\Lambda c_{21}}\right)\\
\Lambda_{Imc_{21}} &= \pi\left((\alpha_{k1}-\alpha 2)(\beta_{13}-1)-\alpha_{k3}(\beta+\beta_{13})\right)\\
&\quad+\sqrt{\xi_{\Lambda c_{21}}^2+\lambda_{\Lambda c_{21}}^2}\,e^{\alpha_2 L_s}\cos\left(\beta k L_s+\theta_{\Lambda c_{21}}\right)
\end{aligned}\right\} \tag{60}$$

$$\left.\begin{aligned}
\Lambda_{Rec_{22}} &= -\pi k\,(\beta_{13}-1)(\beta-\beta_{13})+\alpha_{k3}\tau\,(\alpha_{k1}-\alpha_1)\\
&\quad+\sqrt{\xi_{\Lambda c_{22}}^2+\lambda_{\Lambda c_{22}}^2}\,e^{\alpha_1 L_3}\sin\left(\beta k L_s+\theta_{\Lambda c_{22}}\right)\\
\Lambda_{Imc_{22}} &= \pi\left((\alpha_{k1}-\alpha_1)(1-\beta_{13})-\alpha_{k3}(\beta-\beta_{13})\right)\\
&\quad-\sqrt{\xi_{\Lambda c_{22}}^2+\lambda_{\Lambda c_{22}}^2}\,e^{\alpha_1 L_s}\cos\left(\beta k L_s+\theta_{\Lambda c_{22}}\right)
\end{aligned}\right\} \tag{61}$$

$$\left.\begin{aligned}
\Gamma_{Re} &= \sqrt{\xi_\Gamma^2+\lambda_\Gamma^2}\,e^{\alpha_1 L_3}\sin\left(k\beta L_s+\theta_T\right)\\
&\quad+\sqrt{\xi_\Gamma'^2+\lambda_\Gamma'^2}\,e^{\alpha_2 L_3}\sin\left(k\beta L_s+\theta'_T\right)\\
\Gamma_{Im} &= -\sqrt{\xi_\Gamma^2+\lambda_\Gamma^2}\,e^{\alpha_1 L_3}\cos\left(k\beta L_s+\theta_\Gamma\right)\\
&\quad+\sqrt{\xi_\Gamma'^2+\lambda_\Gamma'^2}\,e^{\alpha_2 L_3}\cos\left(k\beta L_s+\theta'_\Gamma\right)
\end{aligned}\right\} \tag{62}$$

where,

$$\begin{bmatrix}
\xi_{\Lambda c_{11}} & \xi'_{\Lambda c_{11}}\\
\lambda_{\Lambda c_{11}} & \lambda'_{\Lambda c_{11}}\\
\sin\theta_{\Lambda c_{11}} & \sin\theta'_{\Lambda c_{11}}\\
\cos\theta_{\Lambda c_{11}} & \cos\theta'_{\Lambda c_{11}}
\end{bmatrix}$$

$$= \begin{bmatrix} \begin{pmatrix} \pi k(\beta-1)(\beta+\beta_{13}) \\ +\alpha_2\tau(\alpha_1-\alpha_{k3}) \end{pmatrix} & \begin{pmatrix} -\pi k(\beta-\beta_{13})(1+\beta) \\ +\alpha_1\tau(\alpha_{k3}-\alpha_2) \end{pmatrix} \\ \begin{pmatrix} \pi(\alpha_1-\alpha_{k3})(\beta-1) \\ -\alpha_2\pi(\beta+\beta_{13}) \end{pmatrix} & \begin{pmatrix} \pi\alpha_1(\beta-\beta_{13}) \\ +\pi(\alpha_{k3}-\alpha_2)(1+\beta) \end{pmatrix} \\ \frac{\xi_{\Lambda c_{11}}}{\sqrt{\xi_{\Lambda c_{11}}^2+\lambda_{\Lambda c_{11}}^2}} & \frac{\xi'_{\Lambda c_{11}}}{\sqrt{\xi'^2_{\Lambda c_{11}}+\lambda'^2_{\Lambda c_{11}}}} \\ \frac{\lambda_{\Lambda c_{11}}}{\sqrt{\xi_{\Lambda c_{11}}^2+\lambda_{\Lambda c_{11}}^2}} & \frac{\lambda'_{\Lambda c_{11}}}{\sqrt{\xi'^2_{\Lambda c_{11}}+\lambda'^2_{\Lambda c_{11}}}} \end{bmatrix} \tag{63}$$

$$\begin{bmatrix} \xi_{\Lambda c_{12}} & \xi'_{\Lambda c_{12}} \\ \lambda_{\Lambda c_{12}} & \lambda'_{\Lambda c_{12}} \\ \sin\theta_{\Lambda c_{12}} & \sin\theta'_{\Lambda c_{12}} \\ \cos\theta_{\Lambda c_{12}} & \cos\theta'_{\Lambda c_{12}} \end{bmatrix}$$

$$= \begin{bmatrix} \begin{pmatrix} \pi k(1+\beta)(\beta-\beta_{13}) \\ +\alpha_1\tau(\alpha_2-\alpha_{k1}) \end{pmatrix} & \begin{pmatrix} -\pi k(\beta-\beta_{13})(\beta-1) \\ +\alpha_2\tau(\alpha_{k1}-\alpha_1) \end{pmatrix} \\ \begin{pmatrix} \pi(\alpha_{k1}-\alpha_2)(1+\beta) \\ +\pi\alpha_1(\beta+\beta_{13}) \end{pmatrix} & \begin{pmatrix} \pi\alpha_2(\beta_{13}-\beta) \\ +\pi(\alpha_1-\alpha_{k1})(\beta-1) \end{pmatrix} \\ \frac{\zeta_{\Lambda c_{12}}}{\sqrt{\xi_{\Lambda c_{12}}^2+\lambda_{\Lambda c_{12}}^2}} & \frac{\xi'_{\Lambda c_{12}}}{\sqrt{\xi'^2_{\Lambda c_{12}}+\lambda^2_{\Lambda c_{12}}}} \\ \frac{\lambda_{\Lambda c_{12}}}{\sqrt{\xi_{\Lambda c_{12}}^2+\lambda_{\Lambda c_{12}}^2}} & \frac{\lambda'_{\Lambda c_{12}}}{\sqrt{\xi'^2_{\Lambda c_{12}}+\lambda^2_{\Lambda c_{12}}}} \end{bmatrix} \tag{64}$$

$$\begin{bmatrix} \xi_{\Lambda c_{21}} & \xi'_{\Lambda c_{22}} \\ \lambda_{\Lambda c_{21}} & \lambda'_{\Lambda c_{22}} \\ \sin\theta_{\Lambda c_{21}} & \sin\theta'_{\Lambda c_{22}} \\ \cos\theta_{\Lambda c_{21}} & \cos\theta'_{\Lambda c_{22}} \end{bmatrix}$$

$$= \begin{bmatrix} \begin{pmatrix} -\pi k(\beta-\beta_{13})(1+\beta_{13}) \\ -\alpha_{k1}\tau(\alpha_2-\alpha_{k3}) \end{pmatrix} & \begin{pmatrix} -\pi k(\beta+\beta_{13})(1+\beta_{13}) \\ -\alpha_{k1}\tau(\alpha_{k3}-\alpha_1) \end{pmatrix} \\ \begin{pmatrix} -\pi(\alpha_2-\alpha_{k3})(1+\beta_{13}) \\ +\pi\alpha_{k1}(\beta-\beta_{13}) \end{pmatrix} & \begin{pmatrix} -\pi(\alpha_1-\alpha_{k3})(1+\beta_{13}) \\ -\pi\alpha_{k1}(\beta+\beta_{13}) \end{pmatrix} \\ \frac{\zeta_{\Lambda c_{21}}}{\sqrt{\xi_{\Lambda c_{21}}^2+\lambda_{\Lambda c_{21}}^2}} & \frac{\zeta_{\Lambda c_{22}}}{\sqrt{\xi_{\Lambda c_{22}}^2+\lambda_{\Lambda c_{22}}^2}} \\ \frac{\lambda_{\Lambda c_{21}}}{\sqrt{\xi_{\Lambda c_{21}}^2+\lambda_{\Lambda c_{21}}^2}} & \frac{\lambda_{\Lambda c_{22}}}{\sqrt{\xi_{\Lambda c_{22}}^2+\lambda_{\Lambda c_{22}}^2}} \end{bmatrix} \tag{65}$$

$$\begin{bmatrix} \xi_\Gamma & \xi'_\Gamma \\ \lambda_\Gamma & \lambda' \\ \sin\theta_T & \sin\theta'_\Gamma \\ \cos\theta_T & \cos\theta' \end{bmatrix}$$

$$= \begin{bmatrix} \begin{pmatrix} \pi k(\beta+\beta_{13})^2 \\ +\tau(\alpha_2-\alpha_{k1})(\alpha_1-\alpha_{k3}) \end{pmatrix} & \begin{pmatrix} -\pi k(\beta-\beta_{13})^2 \\ -\tau(\alpha_2-\alpha_{k3})(\alpha_1-\alpha_{k1}) \end{pmatrix} \\ \begin{pmatrix} \pi(\beta+\beta_{13}) \\ \times(\alpha_1-\alpha_2+\alpha_{k1}-\alpha_{k3}) \end{pmatrix} & \begin{pmatrix} \pi(\beta-\beta_{13}) \\ \times(\alpha_1-\alpha_2-\alpha_{k1}+\alpha_{k3}) \end{pmatrix} \\ \frac{\xi_\Gamma}{\sqrt{\xi_\Gamma^2+\lambda_\Gamma^2}} & \frac{\xi'_\Gamma}{\sqrt{\xi'^2_\Gamma+\lambda'^2_\Gamma}} \\ \frac{\lambda_\Gamma}{\sqrt{\xi_\Gamma^2+\lambda_\Gamma^2}} & \frac{\lambda'_\Gamma}{\sqrt{\xi'^2_\Gamma+\lambda'^2_\Gamma}} \end{bmatrix} \tag{66}$$

The parameters C_p, C_q, and C_w are given in bellow.

$$C_p = \begin{pmatrix} 1 \\ +\frac{|c_{21}|}{c_{tlm}L_s|r_{c21}+jk|}\begin{pmatrix} e^{\alpha_1 L_s}\sin(k(\beta+1)L_s+\gamma_{c21}-\vartheta_{21}) \\ -\sin(\gamma_{c21}-\vartheta_{21}) \end{pmatrix} \\ -\frac{|c_{22}|}{c_{tlm}L_s|r_{c22}+jk|}\begin{pmatrix} e^{\alpha_2 L_s}\sin(\gamma_{c22}+\vartheta_{22}-k(\beta-1)L_s) \\ -\sin(\gamma_{c22}+\vartheta_{22}) \end{pmatrix} \end{pmatrix} \tag{67}$$

$$C_q = \begin{pmatrix} \frac{1}{G(s+k_w)} \\ -\frac{|c_{21}|}{c_{tlm}L_s|r_{c21}+jk|}\begin{pmatrix} e^{\alpha_1 L_s}\cos(k(\beta+1)L_s+\gamma_{c21}-\vartheta_{21}) \\ -\cos(\gamma_{c21}-\vartheta_{21}) \end{pmatrix} \\ +\frac{|c_{22}|}{c_{tlm}L_s|r_{c22}+jk|}\begin{pmatrix} e^{\alpha_2 L_s}\cos(\gamma_{c22}+\vartheta_{22}-k(\beta-1)L_s) \\ -\cos(\gamma_{c22}+\vartheta_{22}) \end{pmatrix} \end{pmatrix} \tag{68}$$

$$C_w = \begin{pmatrix} \frac{|c_t|^2}{-c_{tlm}} \\ +\frac{|c_{21}|^2\left(e^{2\alpha_1 L_s}-1\right)}{-2c_{tlm}\alpha_1 L_s}+\frac{|c_{22}|^2\left(e^{2\alpha_2 L_s}-1\right)}{-2c_{tlm}\alpha_2 L_s} \\ +2c_{tlm}(1-C_p)+2c_{tRe}(C_q-1/(G(s+k_w))) \\ \frac{-2|c_{21}||c_{22}|}{c_{tlm}L_s\sqrt{M^2+4k^2\beta^2}}\begin{pmatrix} e^{ML_s}\cos\begin{pmatrix} 2k\beta L_s+\gamma_{c21}-\gamma_{c22} \\ -\arctan(2k\beta/M) \end{pmatrix} \\ -\cos\begin{pmatrix} \gamma_{c21}-\gamma_{c22} \\ -\arctan(2k\beta/M) \end{pmatrix} \end{pmatrix} \end{pmatrix} \tag{69}$$

where $\vartheta_{21} = \arctan(k(\beta+1)/\alpha_1)$, $\vartheta_{22} = \arctan(k(1-\beta)/(-\alpha_2))$.

ACOKONWLEDGMENT

The authors thank for China Institute of Atomic Energy to provide the tested loop and ALIP. The original design and manufacture of tested ALIP was accomplished by China Institute of Atomic Energy.

REFERENCES

[1] R. S. Baker and M. J. Tessier, *Handbook of Electromagnetic Pump Technology*. New York, NY, USA: Elsevier, 1987.
[2] *Liquid Metal Cooled Reactors: Experience in Design and Operation*, IAEA, Vienna, Austria, 2007.
[3] B. Zhou, Y. Ji, J. Sun, and Y. L. Sun, "Research on space nuclear reactor power demand analysis," *At. Energy Sci. Technol.*, vol. 54, no. 10, pp. 1912–1923, Oct. 2020.
[4] A. U. Gutierrez and C. E. Heckathorn, "Electromagnetic pumps for liquid metals," Ph.D. dissertation, United States Nav. Postgraduate School, Monterey, CA, USA, 1965.
[5] L. R. Blake, "Conduction and induction pumps for liquid metals," *Proc. IEE-A Power Eng.*, vol. 104, no. 13, pp. 49–67, 1957, doi: 10.1049/pi-a.1957.0021.
[6] B. K. Nashine, S. K. Dash, K. Gurumurthy, U. Kale, V. D. Sharma, R. Prabhakar, M. Rajan, and G. Vaidyanathan, "Performance testing of indigenously developed DC conduction pump for sodium cooled fast reactor," *Indian J. Eng. Mater. Sci.*, vol. 14, pp. 209–214, Jun. 2007.
[7] X. Long, *Theory and Magnetic Design Method of Linear Induction Motor*. Beijing, China: Science, 2006.
[8] S. A. Nasar, I. Boldea, and E. R. Laithwaite, *Linear Motion Electric Machines*. New York, NY, USA: Wiley, 1976.
[9] A. E. Fitzgerald, C. Kingsley, Jr., and S. D. Umans, Eds., *Electric Machinery*, 6th ed. Missouri City, TX, USA: E. A. Jones, 2003.
[10] J. Kwak and H. R. Kim, "Design and preliminary test of an annular linear induction electromagnetic pump for a sodium-cooled fast reactor thermal hydraulic experiment," *J. Nucl. Sci. Technol.*, vol. 54, no. 12, pp. 1292–1299, Dec. 2017, doi: 10.1080/00223131.2017.1365020.
[11] H. R. Kim and Y. B. Lee, "A design and characteristic experiment of the small annular linear induction electromagnetic pump," *Ann. Nucl. Energy*, vol. 38, no. 5, pp. 1046–1052, May 2011, doi: 10.1016/j.anucene.2011.01.008.

[12] H. R. Kim and J. S. Kwak, "MHD design analysis of an annular linear induction electromagnetic pump for SFR thermal hydraulic experimental loop," *Ann. Nucl. Energy*, vol. 92, pp. 127–135, Jun. 2016, doi: 10.1016/j.anucene.2016.01.035.
[13] J. Kwak and H. R. Kim, "Design optimization analysis of a large electromagnetic pump for sodium coolant transportation in PGSFR," *Ann. Nucl. Energy*, vol. 121, pp. 62–67, Nov. 2018, doi: 10.1016/j.anucene.2018.07.019.
[14] B. K. Nashine and B. P. C. Rao, "Design, in-sodium testing and performance evaluation of annular linear induction pump for a sodium cooled fast reactor," *Ann. Nucl. Energy*, vol. 73, pp. 527–536, Nov. 2014, doi: 10.1016/j.anucene.2014.07.026.
[15] B. K. Nashine, P. Sharma, N. Venkatesan, S. K. Kumar, S. Chandramouli, R. R. Prasad, G. Vijayakumar, and P. Selvaraj, "Design, development and testing of a sodium submersible annular linear induction pump for application in sodium cooled fast reactor," *Ann. Nucl. Energy*, vol. 145, Sep. 2020, Art. no. 107494, doi: 10.1016/j.anucene.2020.107494.
[16] L. Wang, Y. Hou, L. Shi, Y. Wu, W. Tian, D. Song, S. Qiu, and G. H. Su, "Experimental study and optimized design on electromagnetic pump for liquid sodium," *Ann. Nucl. Energy*, vol. 124, pp. 426–440, Feb. 2019, doi: 10.1016/j.anucene.2018.10.015.
[17] J. Kwak and H. R. Kim, "Optimization of outer core to reduce end effect of annular linear induction electromagnetic pump in prototype generation-IV sodium-cooled fast reactor," *Nucl. Eng. Technol.*, vol. 52, no. 7, pp. 1380–1385, Jul. 2020, doi: 10.1016/j.net.2019.12.006.
[18] J. Kwak and H. R. Kim, "Development of innovative reactor-integrated coolant system design concept for a small modular lead fast reactor," *Int. J. Energy Res.*, vol. 42, no. 13, pp. 4197–4205, Oct. 2018, doi: 10.1002/er.4177.
[19] S.-H. Seong and S.-O. Kim, "Analyses of annular linear induction pump characteristics using a time-harmonic finite difference analysis," *Nucl. Eng. Technol.*, vol. 40, no. 3, pp. 213–224, Apr. 2008, doi: 10.5516/NET.2008.40.3.213.
[20] H. R. Kim, J. H. Seo, S. H. Hong, H. Y. Nam, and C. Man, "Influences of viscous losses and end effects on liquid metal flow in electromagnetic pumps," in *Proc. Korean Nucl. Soc. Conf.*, Korean Nuclear Society, 1996, pp. 233–240.
[21] W. Xu, J. G. Zhu, Y. Zhang, Y. Li, Y. Wang, and Y. Guo, "An improved equivalent circuit model of a single-sided linear induction motor," *J. IEEE Trans. Veh. Technol.*, vol. 59, no. 5, pp. 2277–2289, Jun. 2010, doi: 10.1109/TVT.2010.2043862.
[22] J. F. Gieras, G. E. Dawson, and A. R. Eastham, "A new longitudinal end effect factor for linear induction motors," *IEEE Trans. Energy Convers.*, vol. EC-2, no. 1, pp. 152–159, Mar. 1987, doi: 10.1109/TEC.1987.4765816.
[23] S. X. Nie, W. M. Ma, W. C. Li, and J. Xu, "Research on thrust ripple of long primary linear induction motors with symmetrical current excited," *Proc. CSEE*, vol. 35, no. 21, pp. 5585–5591, Nov. 2015.
[24] J. K. Dukowicz, "Analysis of linear induction machines with discrete windings and finite iron length," *IEEE Trans. Power App. Syst.*, vol. PAS-96, no. 1, pp. 66–73, Jan. 1977, doi: 10.1109/T-PAS.1977.32308.
[25] K. J. Binns and P. J. Lawrenson, *Analysis and Computation of Electric and Magnetic Field Problems*, 2nd ed. Oxford, U.K.: Pergamon, 1973.
[26] H. R. Kim, Ed., "The design of a small annular linear induction EM pump for the transportation of liquid sodium in the SFR," in *Proc. 21st Int. Conf. Nuclear Eng.*, 2013, p. 6.

ZHENYANG ZHANG (Member, IEEE) was born in Henan, China. He is currently pursuing the Ph.D. degree with the School of Electrical Engineering, Beijing Jiaotong University, Beijing, China. His research interests include analysis, optimal design of new structure electrical machines, electromagnetic filed analysis and simulation of linear induction motor, and performance prediction of annular linear induction pump.

HUIJUAN LIU (Member, IEEE) was born in China. She received the B.S. and M.S. degrees from Tianjin University, Tianjin, China, in 1989 and 1994, respectively, and the Ph.D. degree from the School of Electrical Engineering, Beijing Jiaotong University, in 2009. She worked as a Research Fellow with The Hong Kong Polytechnic University, in 2011 and 2013. Since December 2015, she has been a Professor with Beijing Jiaotong University. Her current research interests include numerical methods of electromagnetic field computation, optimal design and control of high-performance electrical machines and novel electrical motors, such as induction machine, doubly fed brushless machine, and permanent magnetic machine for wind power and other new power source development.

TENGFEI SONG received the M.S. degree from the School of Electrical Engineering, Beijing Jiaotong University, Beijing, in 2017. His research interests include analysis, optimal design of new structure electrical machines, such as vernier machine, and flux-modulated motor for direct-drive applications.

QIAN ZHANG (Student Member, IEEE) was born in China. He is currently pursuing the Ph.D. degree with the School of Electrical Engineering, Beijing Jiaotong University, Beijing, China. His research interests include the optimal design and analysis of novel permanent-magnet motors, linear induction machines, and hardware design of motor drive.

LIXIN YANG was born in China. He received the B.S. degree from Nanjing University of Aeronautics and Astronautics, Nanjing, China, in 1991, and the M.S. and Ph.D. degrees from the Department of Energy and Power Engineering, Tsinghua University, Beijing, China, in 1998 and 2001, respectively. From 2003 to 2005, he was a Postdoctoral Researcher with the University of Science and Technology Beijing. He joined the School of Mechanical, Electronic and Control Engineering, Beijing Jiaotong University, as a Professor, in 2005. From 2009 to 2010, he worked as a Visiting Scholar with the University of Houston, USA. His current research interests include the theory and technology of heat transfer in electromechanical systems, the thermal management of electronic equipment, advanced energy utilization technology, and mechanical engineering.

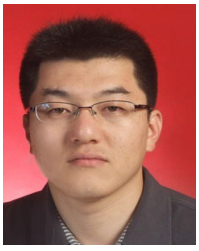

KEMING BI was born in Heilongjiang, in 1983. He received the B.S. degree from the College of Power and Nuclear Engineering, Harbin Engineering University, in 2004. He was hired as a Senior Researcher and the Deputy Director of the Research Laboratory, in 2019. He is currently working with the Reactor Hydraulic Research Laboratory, China Institute of Atomic Energy. Recent years, he is mainly engaged in thermal and hydraulic experimental research related to the nuclear reactors, especially liquid alkali metal cooling reactors. He also develops some special thermal fluid machinery and sensors for the reactor and has more than 20 invention patents.